ACS Catalysis

Research Article

Cite This: ACS Catal. 2019, 9, 11431−11437

pubs.acs.org/acscatalysis

Tuning Electronic Structure and Lattice Diffusion Barrier of Ternary Pt−In−Ni for Both Improved Activity and Stability Properties in Oxygen Reduction Electrocatalysis

Xiaochen Shen,[†,#] Sheng Dai,[‡,#] Yanbo Pan,[†] Libo Yao,[†] Jinlong Yang,[§] Xiaoqing Pan,[‡,∥] Jie Zeng,[§] and Zhenmeng Peng*[,†]

[†]Department of Chemical and Biomolecular Engineering, The University of Akron, Akron, Ohio 44325, United States

[‡]Department of Materials Science and Engineering and [∥]Department of Physics and Astronomy, University of California-Irvine, Irvine, California 92697, United States

[§]Hefei National Laboratory for Physical Sciences at the Microscale, University of Science and Technology of China, Hefei, Anhui 230026, P.R. China

Supporting Information

ABSTRACT: Pt-based alloy electrocatalysts with both good oxygen reduction reaction (ORR) activity and stability have been widely recognized as the key points to realize the fuel cell economy, which however has remained a challenge in the research field. Here, we report an achievement of both improved ORR activity and catalyst stability by incorporating post-transition-metal indium into Pt−Ni alloy nanoparticles. Theoretical simulations suggest the introduction of indium would effectively increase the lattice atom diffusion energy barrier and decrease the particle surface energy, which help with improving the structural stability by decelerating internal Ni leaching and stabilizing the active surface. In the meantime, the electronic structure and consequently ORR activity property of this ternary alloy catalyst would be tuned by controlling its particle composition. Ternary Pt−In−Ni alloy catalysts with controlled particle compositions are synthesized and studied for the ORR properties, which show good agreement with the theoretical study. The $Pt_2In_{0.2}Ni_{1.8}$ nanoparticles with the optimal composition exhibit an initial mass activity of 0.76 A mg_{Pt}^{-1} and retain ∼97.5% of initial activity after accelerated stress test.

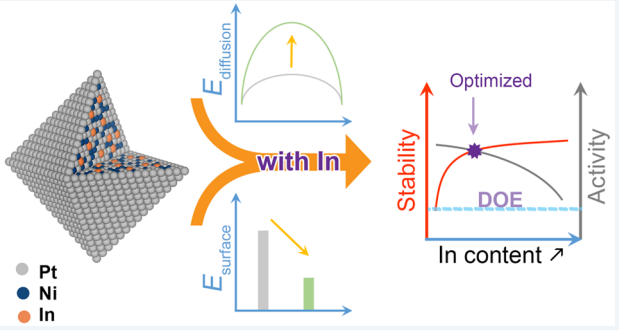

KEYWORDS: *PtInNi alloy, oxygen reduction reaction, electrocatalysis, stability improvement*

INTRODUCTION

The polymer electrolyte membrane fuel cell (PEMFC) technology, being advantageous with high energy efficiency and little emission, has been widely recognized as one viable solution to the realization of a green energy ecosystem. Despite significant research efforts in the past several decades, development of active and durable cathode catalyst for oxygen reduction reaction (ORR) remains a challenge that hinders the application of PEMFCs.[1−4] Current studies have discovered a bunch of alloy catalysts that can exhibit significant improvement in the ORR activity property, in particular, Pt-based alloy nanoparticles such as Pt−Ni, Pt−Co, and Pt−Fe.[5−7] Mechanistic investigations reveal that the electronic interactions between Pt and alloyed metals account for the activity enhancement.[8] However, most of the discovered active alloy catalyst materials were found to suffer from significant structural degradation and thus insufficient stability property, originating from leaching of the non-Pt elements.[9−12] Taking the intensively studied Pt−Ni alloy catalyst for an example, under the ORR condition, surface Ni would dissolve rapidly, which would lead to formation of a thin Pt shell on individual particles. However, the activity decay would not stop afterward, leading to continuous Ni loss and thickening of the Pt shell.[9] This implies the internal lattice Ni atoms can effectively diffuse outward, causing the elemental leaching and consequently a decay in the ORR activity. Cui et al. analyzed a series of Pt−Ni alloy catalyst materials for investigating the leaching issue. The studied Pt_1Ni_1 catalyst was observed with a significant drop of Ni composition to $Pt_1Ni_{0.25}$ in a stability test, with the ORR activity being decayed by 66% in the same course.[9] Ahluwalia et al. reported a similar phenomenon under the membrane electrode assemblies (MEAs) testing condition, demonstrating the crucial stability issue of such alloy catalyst materials for practical applications.[13]

To address this challenge, developing a stratagem that can effectively stabilize the lattice Ni and inhibit its leaching

Received: August 12, 2019
Revised: October 18, 2019
Published: November 5, 2019

DOI: 10.1021/acscatal.9b03430
ACS Catal. 2019, 9, 11431−11437

kinetics is urgent. A plausible approach would be to strengthen the lattice Ni bonding and raise the atom diffusion energy barrier, by which the Ni leaching can be decelerated and thus the ORR activity can be retained. Hence, in this work, we report a strategy to enhance the alloy structure stability property by introducing post-transition-metal element (e.g., In) into the Pt−Ni alloy guided by theoretical simulation screening. This strategy is proved to be effective by preparing ternary Pt−In−Ni alloy nanoparticle catalysts and systematically investigating the ORR activity and stability properties. Our experimental results show that the introduction of In can effectively stabilize lattice Ni from leaching, which significantly improves the catalyst stability. With an optimal composition of $Pt_2In_{0.2}Ni_{1.8}$, a mass activity of 0.76 A mg_{Pt}^{-1} and as high as 97.5% retention of its initial activity after the stability test are obtained, achieving improvement in both the activity and stability properties and confirming effectiveness of our proposed strategy.

EXPERIMENTAL SECTION

Synthesis of $Pt_2In_xNi_{2-x}$/C ($0 \le x \le 1$) Ternary Alloy Nanoparticle Catalysts. Carbon-supported $Pt_2In_xNi_{2-x}$ nanoparticle catalysts were prepared using a dry impregnation-reduction method reported previously.[14] In a typical procedure for preparing $Pt_2In_{0.2}Ni_{1.8}$/C catalyst, the solution of $Pt(acac)_2$ (40 mg, 97%, Sigma-Aldrich), $In(acac)_3$ (4.2 mg, 99.99%, Sigma-Aldrich), and $Ni(acac)_2$ (23.5 mg, 95%, Sigma-Aldrich) in chloroform (3 mL, anhydrous, Sigma-Aldrich) was added drop-wise onto a carbon support (80 mg of XC-72, Cabot Inc.) under vigorous stirring, where the carbon support was thermally pretreated at 300 °C in air overnight prior to use. After impregnation and drying, the obtained precursor mixture was reduced by raising the temperature with a ramping rate of 5 °C/min to 200 °C and maintaining for 1 h under H_2/CO flow (υ_{H_2} = 5 sccm, υ_{CO} = 150 sccm). Ar gas was applied to purge the system after the reduction process to remove residual CO and H_2 gases before the product was collected for characterizations and tests. $Pt_2In_xNi_{2-x}$/C samples with other compositions were synthesized via the same method by adjusting the metal precursor amount.

Preparation of Thin Catalyst Film Electrode. Catalyst ink solution (1 $mg_{catalyst}$/mL) was first prepared by ultrasonically dispersing $Pt_2In_xNi_{2-x}$/C powders in a mixed solvent consisting of deionized (DI) water, isopropanol, and 5 wt % Nafion (V_{water}:$V_{isopropanol}$:$V_{5\%Nafion}$ = 6:4:0.04). Thin catalyst film electrode was fabricated by coating 10 μL of the catalyst ink onto a prepolished glassy carbon rotating disk electrode (RDE) (Φ = 5 mm). The electrode was mounted onto a homemade electrode rotator that rotated at 500 rpm and was dried under a gentle air flow at rotation, resulting in formation of a uniform thin catalyst film on the RDE.

Electrochemical Test. Electrochemical measurements were performed using typical three-electrode configuration on a CHI 760D electrochemical workstation (CH Instruments, Inc.). The thin catalyst film electrode was mounted onto a rotating disk electrode controller (AFMSRCE, Pine Instrument Co.) as the working electrode. A platinum wire was used as the counter electrode and the reference electrode was a HydroFlex electrode (ET070, Edaq Inc.). The reference electrode was calibrated using a home-built reversible hydrogen electrode (RHE). All potentials in this paper were presented with respect to RHE unless stated otherwise.

The electrochemically active surface area (ECSA) measurements of the catalysts were performed in N_2-purged 0.1 M $HClO_4$ solution as described elsewhere.[15] Briefly, a cyclic voltammetry (CV) curve was obtained in the potential range of 0.04−1.0 V at a scan rate of 50 mV/s. The ECSA value was calculated by integrating the hydrogen underpotential deposition (H_{UPD}) signals at ∼0.04−0.40 V with the following equation: $\mathrm{ECSA}\,(\mathrm{cm_{Pt}}^2) = \frac{\int_{E_{low}}^{E_{high}} i\,\mathrm{d}E}{\upsilon Q}$, where i is the current (A), E is the potential (V), E_{low} and E_{high} are lower and upper limits of potential (V) accounting for H_{UPD}, υ is the scan rate (V/s), and Q is the charge density transferred during H_{UPD} (C/cm^2_{Pt}) that has been experimentally determined to be 210 $\mu C/cm^2$ for polycrystalline Pt.[16]

The ORR activity property was measured using linear sweep voltammetry (LSV) from 0.2 to 1.0 V with 10 mV/s potential scan rate at 1600 rpm rotation speed in O_2-saturated 0.1 M $HClO_4$ electrolyte. The solution resistance was determined using electrochemical impedance spectroscopy (EIS) and was employed for iR compensation to obtain accurate ORR activity. The ORR kinetic current density (i_k) at 0.9 V was calculated using the Koutecky−Levich equation: $1/i = 1/i_k + 1/i_{lim} = 1/i_k + 1/(B\omega^{1/2})$, where i is the measured current density (A), i_{lim} is diffusion-limited current density (A), B is a constant, and ω is the angular velocity of RDE ($\omega = 2\pi\nu_{RDE}$ wherein ν_{RDE} is the rotation speed in rpm). The current density showing in CV and LSV plots are normalized to the disk area, while the mass activity (MA) and specific activity (SA) are calculated by normalizing the i_k at 0.9 V to the mass of Pt and ECSA, respectively.

The accelerated stress tests (ASTs) were employed to evaluate the stability of those catalysts in which CV scans cycling between 0.60 and 1.00 V at a scan rate of 50 mV/s for designated numbers in N_2-purged 0.1 M $HClO_4$ were employed. Then the catalyst electrode was cleaned by sweeping the potential between 0 and 1.00 at 10 V/s for another 300 cycles prior to CV and LSV tests for ECSA and ORR activity measurements.

Characterizations. X-ray diffraction (XRD) patterns were recorded on a Bruker AXS Dimension D8 X-ray diffractometer operating at 40 kV and 35 mA (Cu K_α, λ = 0.154184 nm). Transmission electron microscopy (TEM) images were obtained on a JEOL JEM-1230 microscope operating at 120 kV. High-resolution TEM (HRTEM) images were acquired on the scanning transmission electron microscopy (STEM) of a double Cs-corrected JEOL-JEM 3100-R05 microscope at 300 keV. Energy-dispersive X-ray spectroscopy (EDX) data were collected on a Tescan Lyra 3 XMU scanning electron microscope equipped with a quantitative EDX accessory at 25 kV, and the element retention was calculated by assuming the Pt content is constant during AST.

Computational Details. Density functional theory (DFT) calculations were performed using the CAmbridge Serial Total Energy Package .[17] All structures were relaxed prior to any property calculations using Generalized Gradient Approximation and Perdew−Burke−Ernzerhof functional with ultrasoft pseudopotentials.[18] The bulk Ni diffusion was proposed to diffuse to the nearest Ni site and the corresponding transition-state searches were conducted with the complete LST/QST method. The bulk lattice of alloys was optimized before cleaving the (111) facet. The surface was modeled by a five-layer $p(2 \times 2)$ close-packed (111) supercell with a vacuum

DOI: 10.1021/acscatal.9b03430
ACS Catal. 2019, 9, 11431−11437

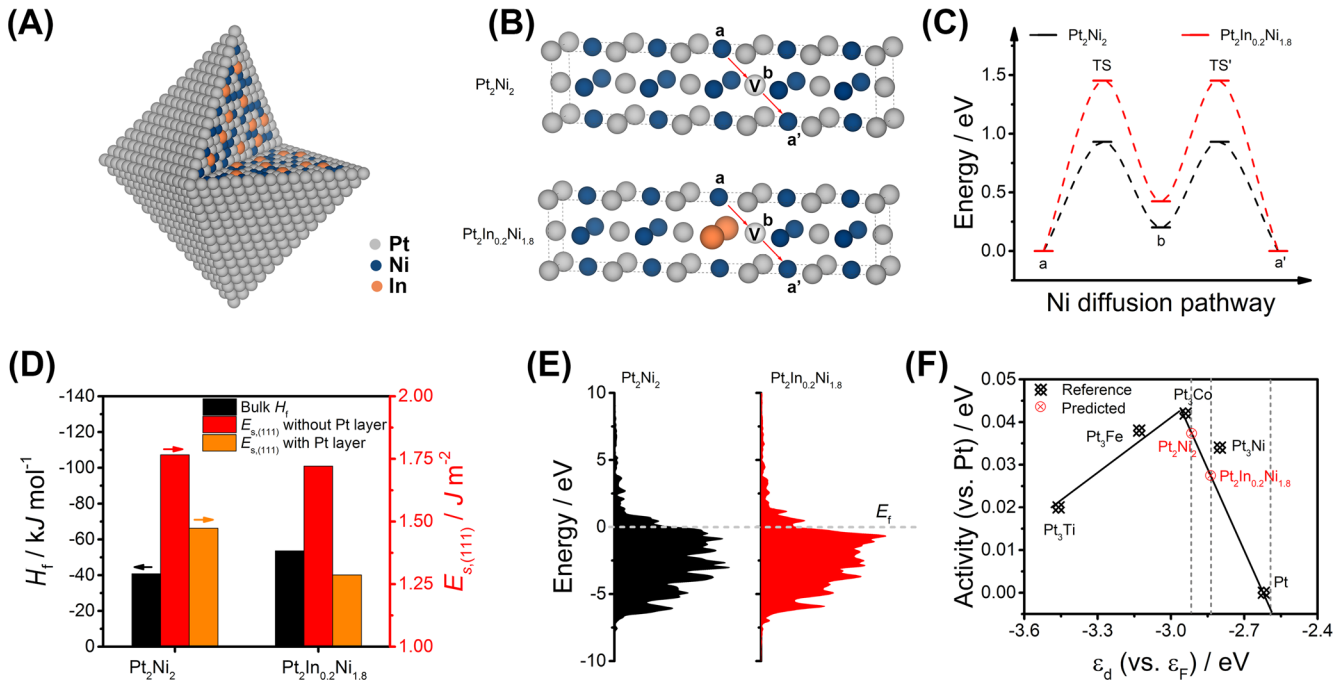

Figure 1. (A) Scheme of the ternary Pt−In−Ni alloy nanoparticle with a Pt layer. (B) Proposed Ni diffusion pathway in the bulk alloy. (C) Ni diffusion pathway energy diagram. (D) Formation energy of bulk $Pt_2In_xNi_{2-x}$ alloy model and the (111) surface energy with/without Pt layer of the $Pt_2In_xNi_{2-x}$ slab model. (E) Projected DOS of the d-electrons of the top layer Pt atoms in the $Pt_2In_xNi_{2-x}$ slab with Pt layer. (F) Predicted ORR activity of the simulated $Pt_2In_xNi_{2-x}$ alloy based on the d-band position (reference data are obtained from ref 20).

layer of 20 Å as shown in Figure S1. The bottom three layers were fixed during the surface relaxation. The plane wave energy cutoff was set as 400 eV with a Monkhorst-pack *k*-point mesh set as 5 × 5 × 1 and a thermal smearing of 0.1 eV. The formation energy (H_f) for bulk alloy was calculated using the following equation: $H_f = E_{alloy} - \Sigma NE_{atom}$, where E_{alloy} is the total energy of bulk alloy unit cell, E_{atom} is the energy of a single atom in its pure bulk lattice, and N is the number of atoms in a bulk alloy unit cell. For the (111) surface energy ($E_{s,(111)}$), it was calculated using the following equation: $E_{s,(111)} = (E_{slab} - ME_{alloy})/2A$, where E_{slab} is the total energy of the surface model, M is the number of bulk alloy unit cells comprising the slab model, and A is the surface area of the slab. Considering the relaxation would cause a difference in the top and bottom surface of the slab model, the E_s of the slab model without surface relaxation was first calculated by acting as the bottom surface energy ($E_{s,bottom}$) in the relaxed slab model. Then for better accuracy, the surface energy of the relaxed slab model is $E_{s,(111),relaxed} = (E_{slab,relaxed} - ME_{alloy} - E_{s,bottom})/A$. For construction of a Pt-covered surface model, the top layer of the corresponding alloy slab was changed to Pt atoms with addition of one more layer at the bottom to keep the stoichiometry unchanged (Figure S1). Thus, the surface energy of the Pt-covered slab is calculated as $E_{s,(111),Pt,relaxed} = (E_{slab,Pt,relaxed} - ME_{alloy} - M'_{Pt,atom} - E_{s,bottom})/A$, where $E_{slab,Pt,relaxed}$ is the total energy of the relaxed Pt-covered slab, M' is the number of Pt atoms in the top Pt layer, and $E_{Pt,atom}$ is the energy of a single Pt atom in the bulk Pt cell. Moreover, the d-band center (ε_d) in this work was defined as the average energy of the occupied d-band and calculated as $\varepsilon_d = \frac{\int_{-\infty}^{0} E\rho_d(E)\,dE}{\int_{-\infty}^{0} \rho_d(E)\,dE}$, where $\rho_d(E)$ is the projected d-band density of states.

RESULTS AND DISCUSSION

DFT simulation screening offers insightful guidance to find suitable third alloying metal element to promote the stability of the Pt−Ni system, where the Pt_2Ni_2 alloy system is taken as a model catalyst. Detailed property modulations have been investigated after the introduction of 5 at. % post-transition-metal In into the system, and simulation results are shown in Figure 1. Considering the alloy possesses face-centered cubic (fcc) structure, which would yield (111)-facet-exposed nanoparticles (Figure 1A), connected fcc unit cells are constructed to simulate the bulk diffusion pathway of lattice Ni element (Figure 1B). From the Ni diffusion energy diagram in Figure 1C, high-energy barriers of Ni diffusion in Pt−In−Ni alloy can be observed ($E_{TS,a-b}$ = 1.45 eV, $E_{TS,b-a'}$ = 1.03 eV), which are significantly higher than those in pure Pt−Ni alloy ($E_{TS,a-b}$ = 0.93 eV, $E_{TS,b-a'}$ = 0.73 eV). Those increased energy barriers indicate that lattice Ni atoms are greatly stabilized after introducing In into the Pt−Ni system. Hence, the leaching of Ni element during the long-term ORR operation are expected to be slowed down to improve its stability. In addition, the formation energies for bulk alloys as in Figure 1D show a noticeable negative shift after introducing In, which also confirms that the bulk of $Pt_2In_{0.2}Ni_{1.8}$ alloy becomes more stable compared to Pt_2Ni_2 bulk.

Because the exposed (111) facet in Pt-based catalysts is the major active surface for ORR catalysis and a thin layer of Pt skin is usually formed on the surface for these catalysts,[19] a series of (111) slab models with/without Pt skin are thus constructed to further study the surface influence of In as shown in Figure S1. The surface energies of these (111) slab models with/without a Pt layer were first calculated and compared in Figure 1D. A clear decrease in the surface energy with In content increase can be observed for both a bare and Pt-layer-covered surface, which proves that In stabilizes the

DOI: 10.1021/acscatal.9b03430
ACS Catal. 2019, 9, 11431−11437

surface of $Pt_2In_{0.2}Ni_{1.8}$ alloy as well. Noticeably, the surface energy of the Pt-layer-covered surface is significantly lower than its counterpart without a Pt layer, indicating further stabilization of such a surface during the ORR process. On the other hand, the electronic structure of $Pt_2In_{0.2}Ni_{1.8}$ alloy would also be tuned with In as shown in Figure 1E. A downshift trend can be seen from the projected density of states (PDOS) of these surface Pt's d-electrons in the $Pt_2In_{0.2}Ni_{1.8}$ slab with Pt layer. According to the surface Pt's d-band center, its ORR activity could be roughly predicted by a volcano plot that was reported previously.[20] Figure 1F shows a slight deviation from the optimized d-band center region and indicates a decrease in ORR activity with the introduction of In. This could be attributed to the nonoptimized overall Pt/In/Ni composition in the current model, which could be further tuned for an optimal d-band center position. Nevertheless, these results manifest that the stability of this Pt−In−Ni ternary alloy system would be significantly improved with corresponding tuned activity for ORR.

Guided by the DFT simulation results, a series of $Pt_2In_xNi_{2-x}/C$ catalysts (x = 0, 0.1, 0.2, 0.5, 1) were synthesized via dry impregnation method.[14] Figure 2A shows

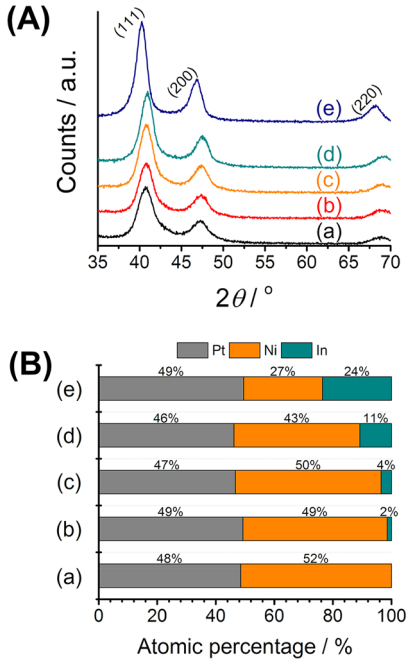

Figure 2. XRD patterns (A) and EDX data (B) of the as-prepared $Pt_2In_xNi_{2-x}/C$ samples: (a) Pt_2Ni_2/C, (b) $Pt_2In_{0.1}Ni_{1.9}/C$, (c) $Pt_2In_{0.2}Ni_{1.8}/C$, (d) $Pt_2In_{0.5}Ni_{1.5}/C$, and (e) $Pt_2In_1Ni_1/C$.

the XRD patterns of these as-prepared $Pt_2In_xNi_{2-x}/C$ samples. Major peaks locate around 40.7° and 47.5° are indexed to the (111) and (200) facets of $Pt_2In_xNi_{2-x}$ alloys, respectively. Noticeably, the diffraction peaks of these samples with low In content (x = 0−0.5) shift toward higher 2θ degree, which seems contradictory to the expected lattice expansion (i.e., toward lower 2θ degree) because of In's larger atom radius compared to that of Ni. This phenomenon can be explained by the improved alloy degree for Pt-based alloy that has been reported previously.[15] Briefly, because the diffraction peak of Pt_2Ni_2/C (e.g., 40.7°) is smaller than its theoretical value (41.3°, PDF No. 065-9445) because of its low alloy degree,[21] the addition of In improves its alloy degree, causing the peaks to shift toward a higher angle, which covers the inverse trend from In's larger atom size. However, when the In concentration reaches 25%, the In atom size becomes a major factor, resulting in a lower 2θ degree shift in diffraction peaks (i.e., $Pt_2In_1Ni_1/C$ sample). Figure 2B summarizes the energy-dispersive X-ray spectroscopy (EDX) element compositions of these $Pt_2In_xNi_{2-x}/C$ samples. And these experimental atomic percentage compositions are consistent with their nominal compositions. Specifically for In content, EDX results match well with the nominal values (in parentheses), that is, 2% (2.5%), 4% (5%), 11% (12.5%), and 24% (25%) for $Pt_2In_{0.1}Ni_{1.9}$, $Pt_2In_{0.2}Ni_{1.8}$, $Pt_2In_{0.5}Ni_{1.5}$, and Pt_2In_1 Ni_1 samples, which further confirms the successful introduction of In into the Pt−Ni alloy system. Additionally, TEM images of these as-prepared $Pt_2In_xNi_{2-x}/C$ catalysts are also shown in Figure 3 and Figure S2, where a typical particle size of 7.6 ± 1.2 nm can be observed for the $Pt_2In_{0.2}Ni_{1.8}/C$ sample in Figure 3A. Noticeably, the octahedral shape of $Pt_2In_xNi_{2-x}$ nanoparticles degrades to a certain extent when In content reaches 25% (Figure S2) while the particle size remains consistent. This degraded morphology could be ascribed to the increased surface In substitution of Ni sites which are crucial for octahedral shape control based on our previous results.[22] High-angle annular dark-field scanning transmission electron microscopy (HAADF STEM) image of one typical $Pt_2In_{0.2}Ni_{1.8}$ nanoparticle is shown in Figure 3B. The d-spacing is measured to be ∼0.217 nm, which can be indexed to the (111) facet of the $Pt_2In_{0.2}Ni_{1.8}$ sample. And its corresponding elemental mapping confirms the homogeneous distribution of Pt, Ni, and In throughout the particle.

The ORR properties of $Pt_2In_xNi_{2-x}/C$ catalysts were evaluated by a series of electrochemical experiments. Figure 4A shows the cyclic voltammetry (CV) curves of these samples, where the hydrogen adsorption regions are used to calculate the electrochemically active surface areas (ECSAs) as summarized in Figure 4B. All the calculated ECSA values are around 40 $m^2\ g_{Pt}^{-1}$ which is a typical value for the Pt−Ni alloy nanoparticles synthesized via dry impregnation method.[23] The linear sweep voltammetry (LSV) results are shown in Figure 5A with calculated activities listed in Figure 5B and Table S1. Noticeably, the ORR activity decreases with increasing In content as predicted in the above DFT simulations, which show that our current Pt/In/Ni composition shifts the d-band center away from the optimal position. Specifically, the mass activity decreases from 0.89 to 0.29 A mg_{Pt}^{-1} when In content reaches 25% (for specific activity, it decreases from 2.31 to 0.69 mA cm_{Pt}^{-2}). However, for the low In content sample like $Pt_2In_{0.2}Ni_{1.8}/C$, despite its slight activity loss, it still possesses a mass activity of 0.76 A mg_{Pt}^{-1}, which is about 4 times higher than that of the current Pt/C catalyst (∼0.20 A mg_{Pt}^{-1}).

On the other hand, because stability is a more significant focus in investigating the In alloyed Pt−Ni catalysts, we implemented accelerated stress tests (ASTs) to evaluate the activity retention of these $Pt_2In_xNi_{2-x}/C$ samples and the results are shown in Figure 6 and Figure S3. The non-In alloyed Pt_2Ni_2/C sample exhibits significant activity loss, where the mass activity reduced to ∼76.8% after 4000 cycles AST experiment (∼73.6% for specific activity), indicating poor stability, whereas improved mass/specific activity retention can be obtained on the In alloyed samples despite the fact that the ECSA values remain unchanged after AST experiments as shown in Figure S4. Interestingly, a higher In content leads to better stability during AST experiments, and the retention

DOI: 10.1021/acscatal.9b03430
ACS Catal. 2019, 9, 11431−11437

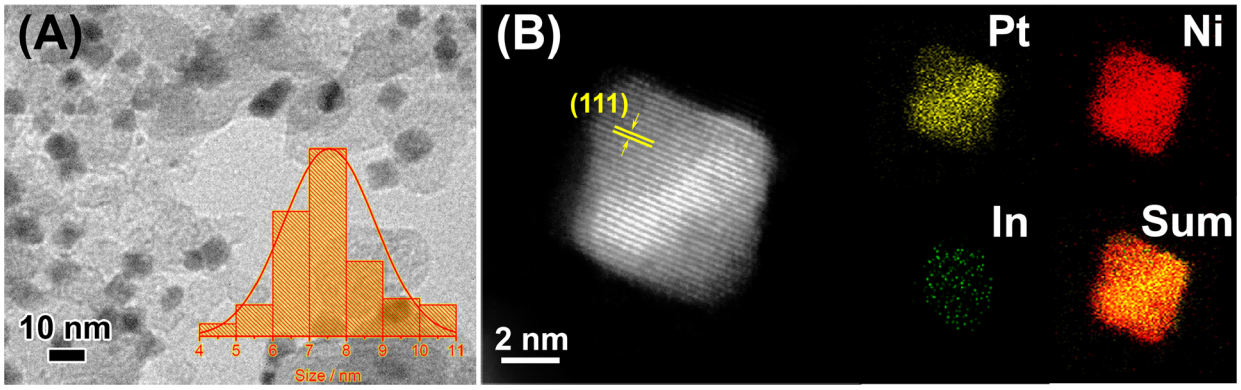

Figure 3. (A) TEM with size distribution (inset) and (B) HAADF STEM images of the as-prepared $Pt_2In_{0.2}Ni_{1.8}/C$ sample with corresponding elemental mapping profile.

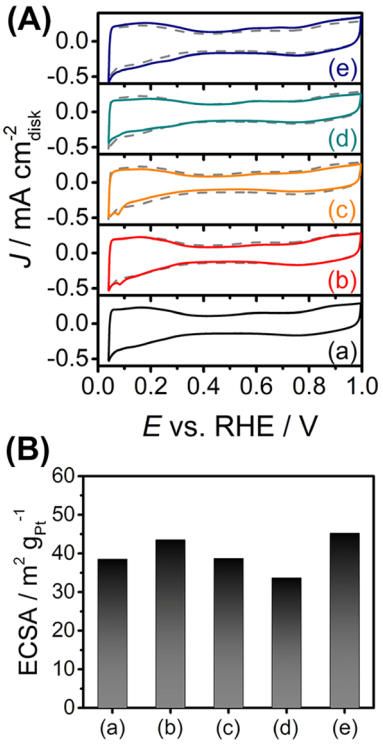

Figure 4. CV curves (A) and ECSA data (B) of the $Pt_2In_xNi_{2-x}$ alloys in N_2-purged 0.1 M $HClO_4$ electrolyte (scan rate: 50 mV/s): (a) Pt_2Ni_2/C, (b) $Pt_2In_{0.1}Ni_{1.9}/C$, (c) $Pt_2In_{0.2}Ni_{1.8}/C$, (d) $Pt_2In_{0.5}Ni_{1.5}/C$, and (e) $Pt_2In_1Ni_1/C$. (Dashed lines indicate the Pt_2Ni_2/C curve for reference.)

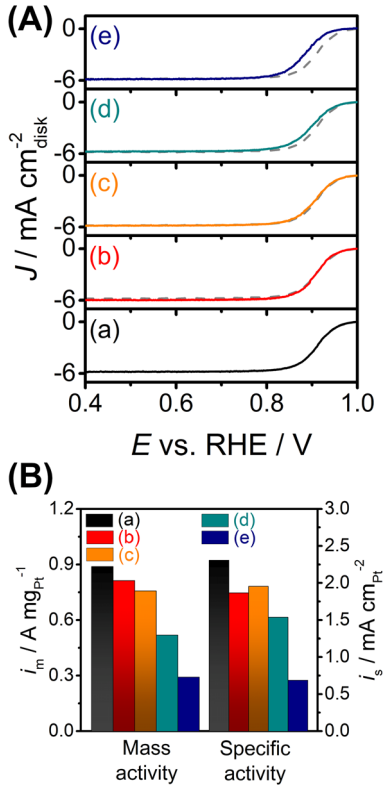

Figure 5. LSV curves (A) and ORR activity at 0.9 V (B) of the $Pt_2In_xNi_{2-x}$ alloys in O_2-saturated 0.1 M $HClO_4$ electrolyte (scan rate: 10 mV/s, rotation speed: 1600 rpm): (a) Pt_2Ni_2/C, (b) $Pt_2In_{0.1}Ni_{1.9}/C$, (c) $Pt_2In_{0.2}Ni_{1.8}/C$, (d) $Pt_2In_{0.5}Ni_{1.5}/C$, and (e) $Pt_2In_1Ni_1/C$. (Dashed lines indicate the Pt_2Ni_2/C curve for reference.).

already exceeds 90% when In content is above 5% as in the $Pt_2In_{0.2}Ni_{1.8}/C$ sample. This result unambiguously demonstrates the effectiveness of In in improving the stability of Pt–Ni alloy ORR catalysts, which matches well with DFT predictions. Considering that although the tuned electronic properties of $Pt_2In_{0.2}Ni_{1.8}/C$ catalyst do not fall in the optimal region, its activity already outperforms many previously reported catalysts as shown in Table S2. Thus, in the current condition, the $Pt_2In_{0.2}Ni_{1.8}/C$ sample achieves optimal overall performance, showing that a mass activity of 0.76 A mg_{Pt}^{-1} and that it retains ~97.5% of its initial activity after AST experiment (~92.3% retention for specific activity) which exhibits superior performance.

The HAADF STEM image of post-AST $Pt_2In_{0.2}Ni_{1.8}/C$ sample in Figure S5A shows that the morphology is well-retained with a slight decrease in facet sharpness compared to that of the fresh sample in Figure 3B. This could be ascribed to the surface restructuring and Pt shell formation because of the leaching of the surface Ni and In atoms during CV cycles, which is the common phenomenon for the PGM alloys.[15] The line scan of post-AST $Pt_2In_{0.2}Ni_{1.8}/C$ sample also confirms the existence of Pt shell as shown in Figure S5B. Moreover, the leaching of bulk Ni elements is slowed down as evidenced by the retained Ni content after AST experiments compared to those as-prepared ones in Figure 6B, which is predicted by increased Ni diffusion energy barrier during DFT screening. And the retention of In is listed in Figure S6 as well. Also, the overall morphology comparison of post-AST samples in Figure

DOI: 10.1021/acscatal.9b03430
ACS Catal. 2019, 9, 11431–11437

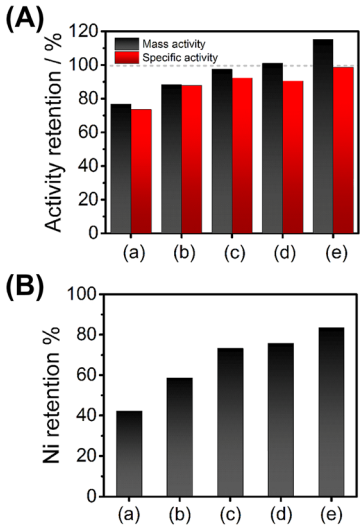

Figure 6. (A) Mass activity/specific activity retention and (B) Ni content retention characterized by EDX during the 4000 cycles AST experiments: (a) Pt_2Ni_2/C, (b) $Pt_2In_{0.1}Ni_{1.9}/C$, (c) $Pt_2In_{0.2}Ni_{1.8}/C$, (d) $Pt_2In_{0.5}Ni_{1.5}/C$, and (e) $Pt_2In_1Ni_1/C$.

S2, where the non-In sample (Pt_2Ni_2/C) shows significant aggregation after AST while the In-alloyed ones still disperse well, further evidences that In stabilizes the nanoparticle surface during AST by lowering its surface energy and prevents the aggregation of these alloy nanoparticles. The well-retained morphology could also contribute to the superior stability of the In-alloyed catalysts. Additionally, we also tested the $Pt_2In_{0.2}Ni_{1.8}/C$ sample with much longer AST cycles, 16 000, and measured its activity retention as shown in Figures S7 and S8, where it still holds a ~76.3% of its initial mass activity (~80.6% for specific activity) as listed in Table S3 with well-retained Ni content and morphology (Figure S9), which enables its route for practical applications.

CONCLUSION

In summary, DFT simulations indicate that introducing In into the Pt−Ni alloy system can significantly decelerate internal Ni diffusion and reduce surface energy to stabilize the catalyst for ORR. The optimal stability and activity were obtained on the $Pt_2In_{0.2}Ni_{1.8}/C$ catalyst as evidenced by a series of experiments. Results show that the optimized $Pt_2In_{0.2}Ni_{1.8}/C$ catalyst possesses a mass activity of 0.76 A mg_{Pt}^{-1} and retains ~97.5% of its initial activity after stress test. The higher Ni content and better morphology that were retained after AST experiment confirm the decelerated Ni diffusion and highly stabilized catalyst surface which agree with DFT results. Our work highlights the effectiveness of post-transition-metal alloying for improving the stability of Pt−Ni alloy electrocatalysts, which offers a new stratagem to improve the alloy stability for practical implementation.

ASSOCIATED CONTENT

Supporting Information

The Supporting Information is available free of charge on the ACS Publications website at DOI: 10.1021/acscatal.9b03430.

Additional TEM and EDX data and DFT models (PDF)

AUTHOR INFORMATION

Corresponding Author

*E-mail: zpeng@uakron.edu (Z.P.).

ORCID

Xiaochen Shen: 0000-0002-7556-8296
Jinlong Yang: 0000-0002-5651-5340
Xiaoqing Pan: 0000-0002-0965-8568
Jie Zeng: 0000-0002-8812-0298
Zhenmeng Peng: 0000-0003-1230-6800

Author Contributions

#X.S. and S.D. contributed equally to this work.

Notes

The authors declare no competing financial interest.

ACKNOWLEDGMENTS

This work was supported by the National Science Foundation CHE-1665265 (Z.P.), the University of Akron (Z.P.), DMR-1506535 (X.P.), and UC Irvine's Office of Research (X.P.).

REFERENCES

(1) Shao, M.; Chang, Q.; Dodelet, J.-P.; Chenitz, R. Recent Advances in Electrocatalysts for Oxygen Reduction Reaction. *Chem. Rev.* **2016**, *116*, 3594−3657.

(2) Sui, S.; Wang, X.; Zhou, X.; Su, Y.; Riffat, S.; Liu, C.-j. A comprehensive review of Pt electrocatalysts for the oxygen reduction reaction: Nanostructure, Activity, Mechanism and Carbon Support in PEM Fuel Cells. *J. Mater. Chem. A* **2017**, *5*, 1808−1825.

(3) Huang, H.; Li, K.; Chen, Z.; Luo, L.; Gu, Y.; Zhang, D.; Ma, C.; Si, R.; Yang, J.; Peng, Z.; Zeng, J. Achieving Remarkable Activity and Durability toward Oxygen Reduction Reaction Based on Ultrathin Rh-Doped Pt Nanowires. *J. Am. Chem. Soc.* **2017**, *139*, 8152−8159.

(4) Liu, C.; Ma, Z.; Cui, M.; Zhang, Z.; Zhang, X.; Su, D.; Murray, C. B.; Wang, J. X.; Zhang, S. Favorable Core/Shell Interface within Co_2P/Pt Nanorods for Oxygen Reduction Electrocatalysis. *Nano Lett.* **2018**, *18*, 7870−7875.

(5) Jiang, K.; Zhao, D.; Guo, S.; Zhang, X.; Zhu, X.; Guo, J.; Lu, G.; Huang, X. Efficient Oxygen Reduction Catalysis by Subnanometer Pt Alloy Nanowires. *Sci. Adv.* **2017**, *3*, No. e1601705.

(6) Chen, Q.; Cao, Z.; Du, G.; Kuang, Q.; Huang, J.; Xie, Z.; Zheng, L. Excavated Octahedral Pt-Co Alloy Nanocrystals Built with Ultrathin Nanosheets as Superior Multifunctional Electrocatalysts for Energy Conversion Applications. *Nano Energy* **2017**, *39*, 582−589.

(7) Zhong, X.; Wang, L.; Zhuang, Z.; Chen, X.; Zheng, J.; Zhou, Y.; Zhuang, G.; Li, X.; Wang, J. Double Nanoporous Structure with Nanoporous PtFe Embedded in Graphene Nanopores: Highly Efficient Bifunctional Electrocatalysts for Hydrogen Evolution and Oxygen Reduction. *Adv. Mater. Interfaces* **2017**, *4*, 1601029.

(8) Stamenkovic, V. R.; Fowler, B.; Mun, B. S.; Wang, G.; Ross, P. N.; Lucas, C. A.; Marković, N. M. Improved Oxygen Reduction Activity on $Pt_3Ni(111)$ via Increased Surface Site Availability. *Science* **2007**, *315*, 493−497.

(9) Cui, C.; Gan, L.; Heggen, M.; Rudi, S.; Strasser, P. Compositional Segregation in Shaped Pt Alloy Nanoparticles and Their Structural Behaviour during Electrocatalysis. *Nat. Mater.* **2013**, *12*, 765.

(10) Colón-Mercado, H. R.; Kim, H.; Popov, B. N. Durability Study of Pt_3Ni_1Catalysts as Cathode in PEM Fuel Cells. *Electrochem. Commun.* **2004**, *6*, 795−799.

(11) Dubau, L.; Durst, J.; Maillard, F.; Guétaz, L.; Chatenet, M.; André, J.; Rossinot, E. Further Insights into the Durability of Pt_3Co/C Electrocatalysts: Formation of "Hollow" Pt Nanoparticles Induced by the Kirkendall Effect. *Electrochim. Acta* **2011**, *56*, 10658−10667.

(12) Cui, C.-H.; Li, H.-H.; Liu, X.-J.; Gao, M.-R.; Yu, S.-H. Surface Composition and Lattice Ordering-Controlled Activity and Durability

DOI: 10.1021/acscatal.9b03430
ACS Catal. 2019, 9, 11431−11437

of CuPt Electrocatalysts for Oxygen Reduction Reaction. *ACS Catal.* **2012**, *2*, 916−924.
(13) Ahluwalia, R. K.; Wang, X.; Peng, J.-K.; Kariuki, N. N.; Myers, D. J.; Rasouli, S.; Ferreira, P. J.; Yang, Z.; Martinez-Bonastre, A.; Fongalland, D.; Sharman, J. Durability of De-Alloyed Platinum-Nickel Cathode Catalyst in Low Platinum Loading Membrane-Electrode Assemblies Subjected to Accelerated Stress Tests. *J. Electrochem. Soc.* **2018**, *165*, F3316−F3327.
(14) Zhang, C.; Hwang, S. Y.; Trout, A.; Peng, Z. Solid-State Chemistry-Enabled Scalable Production of Octahedral Pt−Ni Alloy Electrocatalyst for Oxygen Reduction Reaction. *J. Am. Chem. Soc.* **2014**, *136*, 7805−7808.
(15) Zhang, C.; Sandorf, W.; Peng, Z. Octahedral Pt_2CuNi Uniform Alloy Nanoparticle Catalyst with High Activity and Promising Stability for Oxygen Rreduction Reaction. *ACS Catal.* **2015**, *5*, 2296−2300.
(16) Tian, N.; Zhou, Z.-Y.; Sun, S.-G.; Ding, Y.; Wang, Z. L. Synthesis of Tetrahexahedral Platinum Nanocrystals with High-Index Facets and High Electro-Oxidation Activity. *Science* **2007**, *316*, 732−735.
(17) Clark, S. J.; Segall, M. D.; Pickard, C. J.; Hasnip, P. J.; Probert, M. I. J.; Refson, K.; Payne, M. C. First Principles Methods using CASTEP. *Z. Kristallogr. Cryst. Mater.* **2005**, *220*, 567.
(18) Perdew, J. P.; Burke, K.; Ernzerhof, M. Generalized Gradient Approximation Made Simple. *Phys. Rev. Lett.* **1996**, *77*, 3865−3868.
(19) Chen, S.; Niu, Z.; Xie, C.; Gao, M.; Lai, M.; Li, M.; Yang, P. Effects of Catalyst Processing on the Activity and Stability of Pt−Ni Nanoframe Electrocatalysts. *ACS Nano* **2018**, *12*, 8697−8705.
(20) Stamenkovic, V. R.; Mun, B. S.; Arenz, M.; Mayrhofer, K. J. J.; Lucas, C. A.; Wang, G.; Ross, P. N.; Markovic, N. M. Trends in Electrocatalysis on Extended and Nanoscale Pt-Bimetallic Alloy Surfaces. *Nat. Mater.* **2007**, *6*, 241.
(21) Do, C. L.; Pham, T. S.; Nguyen, N. P.; Tran, V. Q.; Pham, H. H. Synthesis and Characterization of Alloy Catalyst Nanoparticles PtNi/C for Oxygen Reduction Reaction in Proton Exchange Membrane Fuel Cell. *Adv. Nat. Sci: Nanosci. Nanotechnol.* **2015**, *6*, 025009.
(22) Shen, X.; Zhang, C.; Zhang, S.; Dai, S.; Zhang, G.; Ge, M.; Pan, Y.; Sharkey, S. M.; Graham, G. W.; Hunt, A.; Waluyo, I.; Miller, J. T.; Pan, X.; Peng, Z. Deconvolution of Octahedral Pt_3Ni Nanoparticle Growth Pathway from In Situ Characterizations. *Nat. Commun.* **2018**, *9*, 4485.
(23) Zhang, C.; Hwang, S. Y.; Peng, Z. Size-Dependent Oxygen Reduction Property of Octahedral Pt−Ni Nanoparticle Electrocatalysts. *J. Mater. Chem. A* **2014**, *2*, 19778−19787.

DOI: 10.1021/acscatal.9b03430
ACS Catal. 2019, 9, 11431−11437